

# Local Electrochemical Measurements by 3D Printed Sf-MDC Equipped with Optical Microscope\*

Kei Sakata\*\*, Muhammad Bilal\*\*\*, Masatoshi Sakairi\*\*\*\* and Takuya Murata\*\*\*\*\*

A 3D printed solution flow type micro droplet cell (Sf-MDC) was attached to an optical microscope, making it possible to switch between the lens and Sf-MDC at the same observation/measurement area. Using this setup, precipitates in an Al-Si alloy were investigated. Open circuit potential measurements and potentiodynamic measurements were conducted at various surface areas of the Al-Si alloy. The precipitate area ratio affected open circuit potentials and anodic currents. This 3D printed Sf-MDC can be applied for the electrochemical investigation of precipitates in Al-Si alloy.

**Keywords:** 3D printed solution flow type micro droplet cell (Sf-MDC), Al-Si alloy, electrochemical investigation

## 1. Introduction

Metals have been shown to exhibit advanced properties such as high strength, high corrosion resistance, and wear resistance with material non-uniformities strongly influencing these properties. To investigate material non-uniformities, improvements in the resolution of analysis of materials are necessary, however. Recently, high resolution electrochemical measurement technology is attracting attention, and the electrochemical measurement technique for micro areas with electrochemical microcells<sup>1)~8)</sup> is a candidate for improvements in resolution. Electrochemical microcells are classified into two types, meniscus and gasket types, differentiated by the structural differences between the capillary tip and sample arrangement<sup>9), 10)</sup>. Meniscus type cells form electrolyte droplets between the sample and the cell, and the distance from the tip of the capillary to the sample is kept constant during measurements. During the electrochemical reaction, the area where the formed droplet is in contact with the sample acts as a working electrode. The area of the droplet is maintained by the balance between the

surface tension and gravity. One application of the meniscus type cell, scanning electrochemical probe microscopy has attracted attention<sup>11)~13)</sup> as it is possible to observe the electrochemical reaction of the electrode/solution interface with high resolution. In gasket type cells, the tip of the capillary is in contact with the sample surface, and the inside of the capillary is filled with the electrolyte, a silicone rubber attachment to the tip of the capillary acts as a gasket preventing the solution from leaking. Böhni et al. equipped a gasket-type electrochemical microcell to an optical microscope and investigated the pitting corrosion process of stainless steel<sup>14)</sup>. However, when the electrode reaction increases, with both meniscus and gasket type electrochemical microcells, the solution concentration changes near the sample surface become very large, and a concentration gradient is generated in the capillary, which makes it impossible to perform accurate measurements and to control the chemical reactions. To improve on this, Lohrengel et al. developed a solution flow type electrochemical microcell equipped with  $\theta$ -type glass capillary<sup>15), 16)</sup>. In this cell, solution supply and drainage are achieved using two channels. Fushimi et al.

\* This paper has been published in Journal of The Electrochemical Society, **168** (2021), 061505.

\*\* Japan International Consultants for Transportation Co., Ltd.

\*\*\* Department of Chemistry, Lehigh University

\*\*\*\* Faculty of Engineering, Hokkaido University. Ph. D. (Eng.)

\*\*\*\*\* Research & Development Division, UACJ Corporation

developed a solution flow type micro droplet cell (Sf-MDC)<sup>17</sup>. The Sf-MDC has a coaxial double tube structure with two different diameters. Solution is supplied from the inner capillary and the solution is suctioned by the outer capillary. Sakairi et al. used Sf-MDC to control the area and thickness of anodic oxide film on aluminum<sup>18)–20)</sup>. Hashizume et al. investigated the mechanism of stress corrosion cracking at joints using Sf-MDC<sup>21)</sup>. Sf-MDC can be applied electrochemically in a variety of microscopic regions. However, the structure of the conventional Sf-MDC device is very complicated and difficult to manufacture, and in recent years, Sf-MDC devices have been fabricated using 3D printing. Kollender et al. were the first to produce a flow-type scanning droplet cell microscope using a 3D printer<sup>22)</sup>. They also fabricated a multi-scanning droplet cell microscope and used it to study anodized titanium surfaces<sup>23)</sup>. Summers et al. fabricated a solution flow type microcell where the tip can be replaced according to the application<sup>24)</sup>. Bilal et al. performed area selective aluminum anodization and nickel/copper electrodeposition using a Sf-MDC fabricated by a 3D printer<sup>25)–27)</sup>. In addition, the conventional Sf-MDC is long in the vertical direction, with the result that it is difficult to equip it to a microscope, and it is difficult to precisely control the measured area. In this paper, a novel configuration of an Sf-MDC was fabricated using a 3D printer, equipped with an optical microscope, and local electrochemical measurements were performed to investigate the size of the Si related precipitates on the electrochemical behavior of an aluminum alloy.

## 2. Experimental

### 2.1 Sample

To investigate effect of the size of Si related precipitates, an in-house produced Al-20mass% Si alloy was used as the sample. A heat treatment was carried out to enlarge the precipitate. Samples were connected to a conductive wire and embedded in epoxy resin leaving an exposed surface. After polishing to #4000 with SiC paper, the specimen was ultrasonically cleaned in highly purified water and 99.5% ethanol for 300 s.

### 2.2 Design of Sf-MDC

The Sf-MDC was designed using computer-aided design (CAD) software (Blender 2.80). The designed Sf-MDC was made from a clear photopolymer resin (Formlabs, FLGPCL04) by a 3D printer (Formlabs, Form 2). The stacking pitch of 3D printing was 0.05 mm. **Fig. 1** shows (a) the wire frame, and (b) a schematic outline of the Sf-MDC. The solution is supplied to the inner capillary through the solution inlet at the top and is suctioned from the outer capillary to the solution outlet (Fig. 1 (a)). The diameter of the inner capillary is 0.65 mm, the diameter of the outer capillary is 1.56 mm, with the height of the cell 15 mm (Fig. 1 (a)). A platinum wire is inserted as a counter electrode and an Ag/AgCl wire is inserted as a reference electrode in the cell (Fig. 1 (b)). The inserted Ag/AgCl wire was obtained by anodizing a silver wire in hydrochloric acid. The inner capillary supplied solution to the droplet and the outer capillary collected solution from the formed droplet. A typical solution flow type electrochemical microcell<sup>22), 23)</sup> supplied solution from one side of the droplet and aspirated it from the other side, while this cell supplied solution from the center of the droplet and pumped solution from the periphery of the formed droplet.

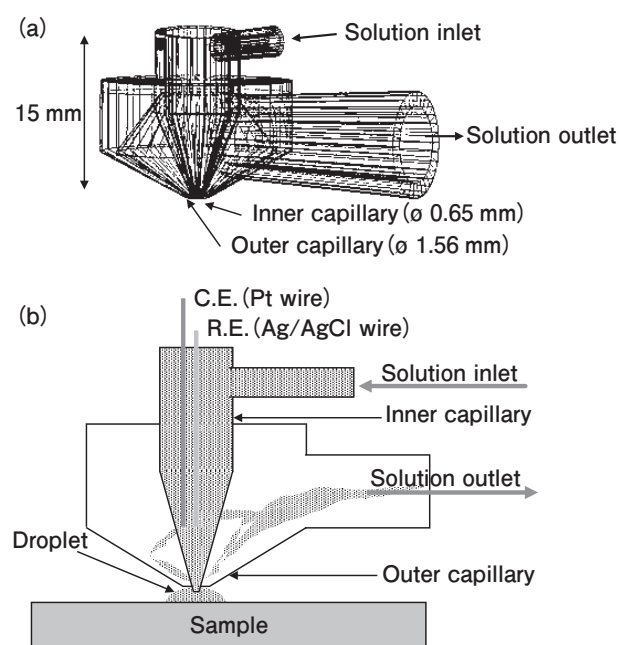


**Fig. 1** (a) Wire frame design for 3D printed Sf-MDC with coaxial dual capillary. (b) Schematic representation of the cell.

### 2.3 Open circuit potential and potentiodynamic polarization measurements

The Sf-MDC was attached to an optical microscope. The solution inlet was connected to a pump by a silicone tube (diameter ; 2 mm) and the solution outlet was connected to an aspirator (ULVAC KIKO Inc., MDA-015)<sup>25</sup>). The flow rate of the solution was controlled at  $1.0 \times 10^{-3} \text{ cm}^3 \text{ s}^{-1}$  using a pump (ATTO Corp., SJ-1211), and aspirated at around 90 kPa with an aspirator. The solution was  $10 \text{ mol m}^{-3} \text{ NaCl}$ . After selecting a measurement area on the sample surface with the microscope, a droplet was formed by the Sf-MDC. The open circuit potential (OCP) was measured for 900 s. From (OCP -200 mV) to (OCP + 400 mV), potentiodynamic polarization measurements were performed at a scanning rate at  $60 \text{ mV min}^{-1}$ . A noise filter with a cutoff frequency of 10 kHz was used to reduce the noise.

### 2.4 Immersion test

The sample was polished to #4000 with SiC paper and then buff polished to further smoothen the surface. After ultrasonic cleaning in highly purified water and 99.5% ethanol for 300 s each, the sample was immersed in  $10 \text{ mol m}^{-3} \text{ NaCl}$  for 7 d. The temperature was maintained at 303 K.

### 2.5 Observation and analysis.

The surface of the sample after the test was observed with an optical microscope and a scanning electron microscope, SEM (JEOL Ltd., JSM-6510LA). The images obtained from the optical microscope were analyzed using image analysis software (Image J 1.53a), and the precipitate area ratio was calculated. The surface of the sample was analyzed using an energy dispersive X-ray spectroscope, EDS (JEOL Ltd., JSM-6510LA) and a laser scanning confocal microscope, LSCM (Lasertec Co., ILM21D).

## 3. Results and Discussions

### 3.1 Fabrication of the Sf-MDC

**Fig. 2** (a) and (b) illustrate the Sf-MDC fabricated in this study, and (c) shows the photograph of the Sf-MDC equipped with an optical microscope. The Sf-MDC designed by CAD software was fabricated

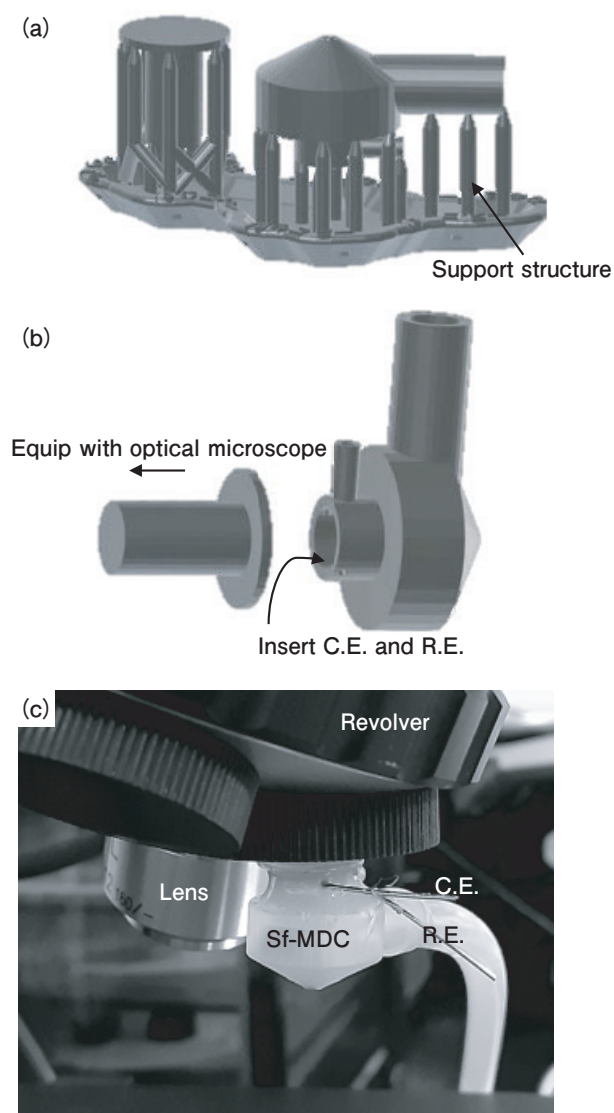


**Fig. 2** Illustration of the 3D printed parts of Sf-MDC (a) with support structure and (b) detached from the support structure. (c) Optical image of Sf-MDC attached to the optical microscope.

using a 3D printer with the support structure shown in Fig. 2 (a). Without this support structure, Sf-MDC with coaxial dual capillaries cannot be printed accurately. Since the fabricated Sf-MDC is affected by the printing direction and the resolution of the 3D printer<sup>25), 26)</sup>, the fine structure (inner capillary, solution inlet tube etc.) was inspected carefully during the manufacture. After confirming that the structure is printed properly, the Sf-MDC was washed in 2-propanol and allowed to cure for 30 minutes. After that, the counter electrode and the reference electrode were inserted into the inner capillary and then attached to an optical microscope (Fig. 2 (b)). The solution inlet was connected to the solution pump via the silicone tube and the solution outlet was

connected to the aspirator. Using the revolving carousel of the optical microscope, it is possible to switch between the lens and the Sf-MDC at the same observation/measurement area (Fig. 2 (c)).

### 3.2 Open circuit potential and potentiodynamic polarization measurements

Fig. 3 shows the results of (a) the open circuit potential and (b) the potentiodynamic polarization measured by the fabricated Sf-MDC at two selected areas. It verifies that the open circuit potentials and polarization curves are different in two different areas. Similar open circuit potentials are observed in both areas at the initial stage of the open circuit

potential measurements in Fig. 3 (a). After some time, the open circuit potential shifts to the negative direction and there are random fluctuations. The time that the open circuit potential shift is observed at Area 1 is later than that of Area 2. The fluctuations observed in Fig. 3 (a) may relate to localized corrosion events such as metastable pitting<sup>28</sup>). Chiba et al. reported that Al matrix around Si phases was preferentially dissolved<sup>29</sup>). The number of fluctuations observed in Area 1 is smaller than that observed in Area 2. These results may relate to size or area ratio of the Si related precipitates. The cathodic current observed at Area 1 is larger than that observed at Area 2, while the anodic current is opposite (Fig. 3 (b)).

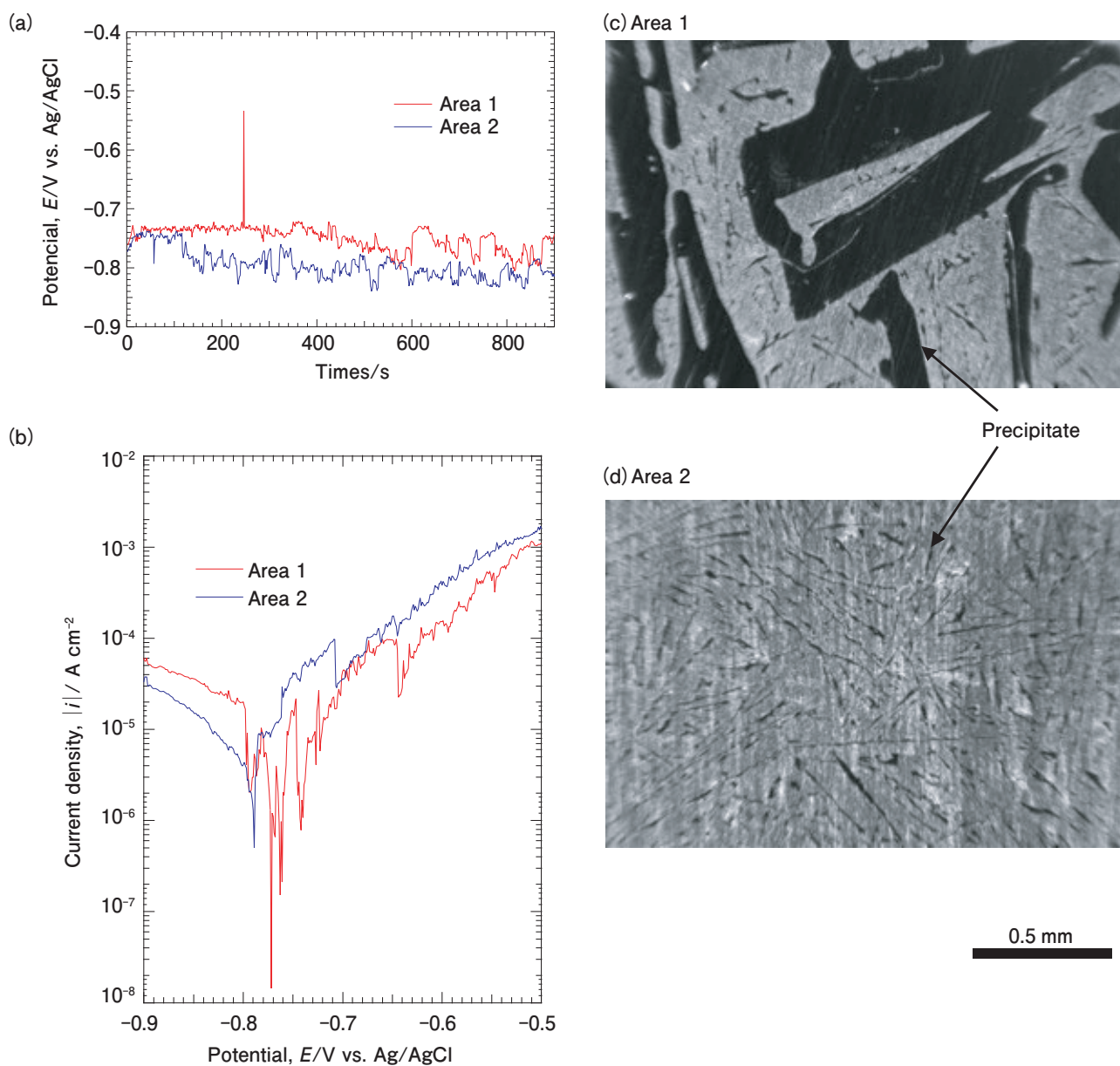


Fig. 3 (a) Open circuit potential and (b) polarization curves measured with the 3D printed Sf-MDC. Optical microscope images of the measured area with different precipitate area ratios; (c) Area 1 is with a 49% precipitated area and (d) Area 2 is with a 9% precipitated area.

From this result and the literature<sup>29</sup>, Si related precipitates may act as cathodic sites and the Al substrate acting as the anodic sites. The observed polarization behavior causes the open circuit potential of Area 1 to be higher than that of Area 2.

To confirm the size of the Si related precipitates on the electrochemical behavior, the sample surface after the tests were observed by an optical microscope. Fig. 3 (c) and (d) show optical microscope images of Areas 1 and 2 after the measurements. Large black segregated precipitates can be seen in Area 1, these large precipitates are not observed in Area 2. From the optical microscope images, the area ratio of black precipitates was calculated using Image J software. The calculated area ratio of black precipitates in Area 1 was 49% and that in Area 2 was 9%. The difference in the area ratios of the precipitates could be a cause of the difference in the open circuit potentials and in the polarization curves. To clarify the relationship between the precipitate area ratio and electrochemical measurement results, similar measurements were conducted at 10 different positions.

**Fig. 4** shows (a) the average open circuit potentials between 700 s and 900 s from open circuit potential measurements, and (b) is the average anodic current between  $-0.66$  and  $-0.64$  V obtained from the potentiodynamic polarization measurements as a function of the precipitate area ratio. The average open circuit potential increases with increasing precipitate area ratio. It can be seen that the average anode current decreases with increasing precipitate area ratios. It is known that Si is a nobler element than Al, and it has been reported that the amount of Si in the Al-Si alloy affected the electrochemical behavior<sup>30</sup>. In the experiment here, the differences in the amount of Si on the measured surfaces could also have affected the open circuit potentials and anodic currents.

### 3.3 Immersion tests

To establish the reason why the anodic current decreases with the precipitate area ratio, immersion tests and surface observations were conducted. **Fig. 5** (a) shows an optical microscope image before the immersion test, and (b) after the test. It clearly shows that there are large precipitates and small

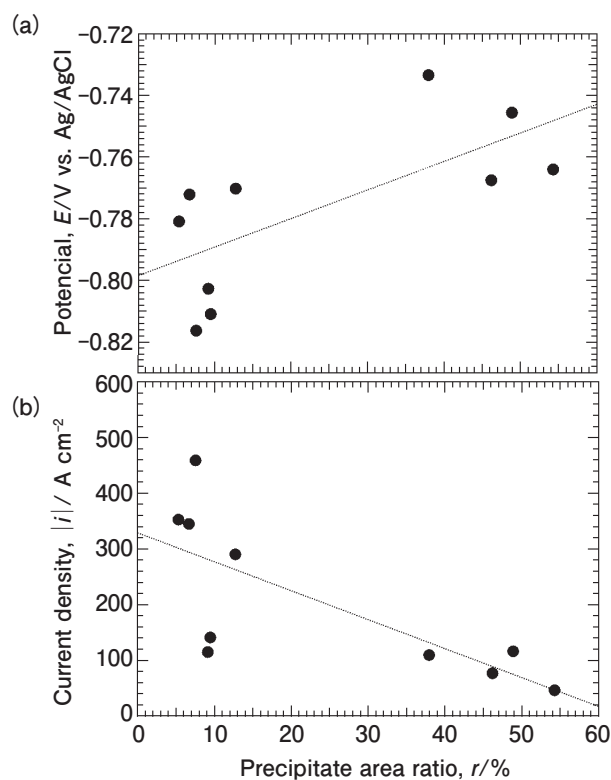


**Fig. 4** (a) Average open circuit potentials between 700 s and 900 s and (b) average anodic currents between  $-0.66$  and  $-0.64$  V as a function of precipitate area ratios.

precipitates (Fig. 5 (a)). After the immersion test, the image is all black except for the large precipitates (Fig. 5 (b)). The brightness of the optical microscope image is affected by the flatness or height of the sample. The focusing conditions were checked and it was confirmed that the dark areas are lower than the bright areas. From the optical microscope observation, the initial smooth surface develops irregularities through the 7 d immersion test. Due to the limitations of the optical microscope observations, a more precise observation of the surface morphology was performed using LSCM.

**Fig. 6** shows a 3-D height image of the same area as in Fig. 5. It is confirmed that the large precipitates are higher than other areas and the surface roughness (RMS) was about  $8.5 \mu\text{m}$ . Since the RMS before the test was about  $0.1 \mu\text{m}$ , the results show that the surface became more uneven through the 7 d immersion test. This LSCM result suggests that Al matrix preferentially dissolved and that the large precipitates appeared. Further, other areas than those with large precipitates are high. These parts do not relate to the location of the precipitates in the optical

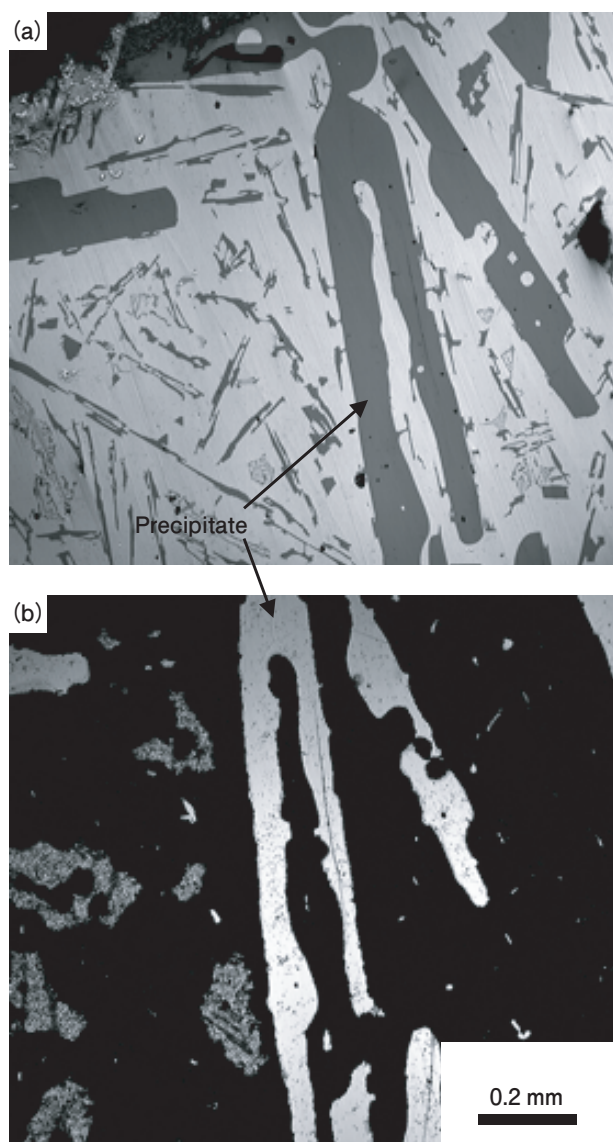


**Fig. 5** Optical microscope images of sample (a) before immersion test and (b) after the test.

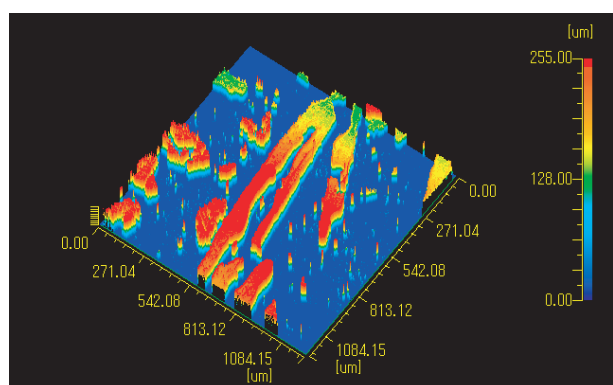


**Fig. 6** 3-D height displaying the area in Figure 5 after the immersion test.

microscope image before the test (Fig. 5(a)). In order to elucidate the reasons, the area was observed and analyzed using SEM and EDS.

**Fig. 7** shows (a) SEM image and EDS element

mapping results for (b) Al, (c) Si, and (d) O. The EDS analysis shows that the precipitates contain Si and that the other areas contain Al and O. The reason for the height differences could be that the Al matrix was easily dissolved through the immersion test and that the large Si-rich precipitate was little dissolved. In addition, the higher areas suggest that the large precipitates in Fig. 6 are mainly composed of Al and O. This result suggests that the high areas are corrosion products of Al. As Chiba et al.<sup>29)</sup> reported, preferential dissolution of Al substrate formed corrosion products, resulting in the formation of the higher areas.

Focusing on the fact that the Al matrix is easier to dissolve than the Si-rich precipitates, the reason why the anodic current becomes smaller with increasing the precipitate area ratio can be understood. **Fig. 8** shows a schematic representation of the Al dissolution and anodic current with precipitate area ratios. When the precipitate area ratio is low, the area where Al can be dissolved is large and the anode current is large. When the precipitate area ratio is high, the area where Al can be dissolved is small and the anode current is smaller. The solubility difference between Al matrix and Si-rich precipitates causes the anodic current to change depending on the precipitate area ratio.

#### 4. Conclusions

An Sf-MDC was fabricated by a 3D printer and attached to an optical microscope. Using the revolving carousel of the optical microscope, it was possible to switch between the lens and Sf-MDC at the same observation/measurement area. Precipitates of Al-Si alloy were investigated by the Sf-MDC. As the precipitate area ratio at the measured area increased, the open circuit potential increased and the anodic current decreased. From the surface observations after the immersion test, it was found that the Al matrix is more soluble than the Si-rich precipitate. It was assumed that the difference in the area where Al could be dissolved was the reason of the change in the anodic current depending on the precipitate area ratio.

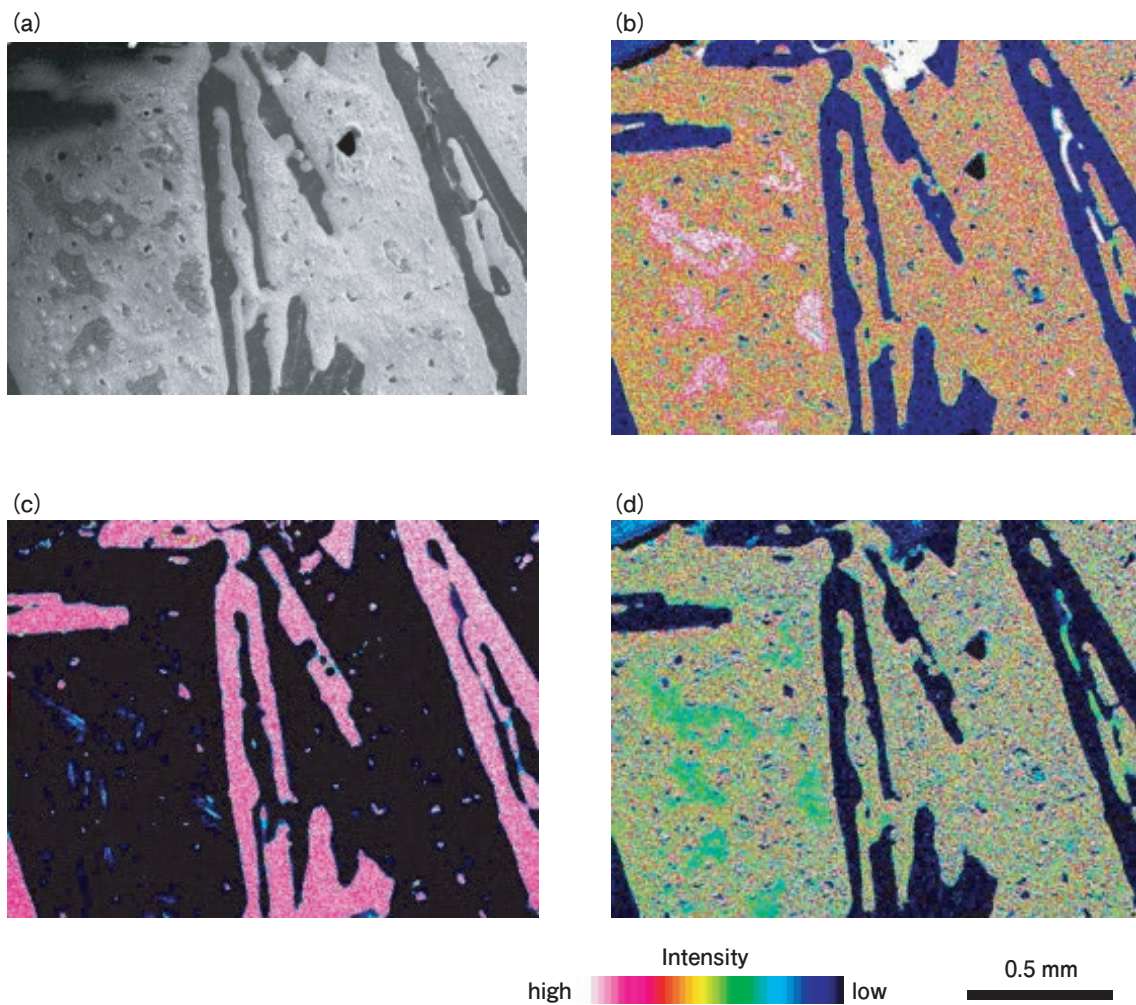


Fig. 7 (a) SEM image and elemental mapping by EDS at the same area as in Figure 5, (b) Al, (c) Si, and (d) O.

Precipitate area ratio	Low	High
Al dissolution area	<p>Large</p>	<p>Small</p>
Anodic current	Large	Small

Fig. 8 Schematic representation of relationship between precipitate area ratios and measured anodic current by potentiodynamic polarization with the 3D printed Sf-MDC. The precipitate is Si rich and the matrix is Al rich.

### Acknowledgments

SEM and LSCM observation of this work was conducted at the Laboratory of XPS analysis, Joint use facilities, Hokkaido University.

### REFERENCES

- 1) C. Garcia, F. Martin, P. de Tiedra, Y. Blanco and M. Lopez: Corros. Sci., **50** (2008) 1184-1194.
- 2) T. Suter and H. Böhni: Electrochim. Acta, **43** (1998) 2843-2849.
- 3) M. Sakairi, T. Nakayama, T. Kikuchi, S. Hasizume and K. Fushimi: ECS Trans., **52** (2009) 281-290.
- 4) A. W. Hassel and M. M. Lohrengel: Electrochim. Acta, **42** (1997) 3327-3333.

- 5) C. Rosenkranz, M. M. Lohrengel and J. W. Schultze: *Electrochim. Acta*, **50** (2005) 2009–2016.
- 6) B. Walther, J. Schilm, A. Michaelis and M. M. Lohrengel: *Electrochim. Acta*, **52** (2007) 7732–7737.
- 7) A. Schreiber, C. Rosenkranz and M. M. Lohrengel: *Electrochim. Acta*, **52** (2007) 7738–7745.
- 8) M. Sakiri, Y. Goto, K. Fushimi, T. Kikuchi and H. Takahashi: *Electrochemistry (Tokyo)*, **78** (2010) 118–121.
- 9) M. M. Lohrengel: *Electrochim. Acta*, **42** (1997) 3265–3271.
- 10) H. Böhni, T. Suter, and A. Schreyer: *Electrochim. Acta*, **40** (1995) 1361–1368.
- 11) J. P. Kollender, A. I. Mardare and A. W. Hassel: *Chemphyschem*, **14** (2013) 560–567.
- 12) C. L. Bentley, M. Kang and P. R. Unwin: *Curr. Opin. Electrochem.*, **6** (2017) 23–30
- 13) T. Tarnev, H. B. Aiyappa, A. Botz, T. Erichsen, A. Ernst, C. Andronesco and W. Schuhmann: *Angew. Chem. Int. Ed.*, **58** (2019) 14265–14269.
- 14) H. Böhni, T. Suter, and F. Assi: *Surf. Coat. Technol.*, **130** (2000) 80–86.
- 15) M. M. Lohrengel, C. Rosenkranz, I. Klüppel, A. Moehring, B. Van den Bossche and J. Deconinck: *Electrochim. Acta*, **49** (2004) 2863–2870.
- 16) M. M. Lohrengel, I. Klüppel, C. Rosenkranz, H. Bettermann and J. W. Schultze: *Electrochim. Acta*, **48** (2003) 3203–3211.
- 17) K. Fushimi, S. Yamamoto, R. Ozaki and H. Habazaki: *Electrochim. Acta*, **53** (2008) 2529–2537.
- 18) M. Sakairi, T. Yamaguchi, T. Murata and K. Fushimi: *ECS Trans.*, **50** (2013) 255–262.
- 19) M. Sakairi, F. Nishino and R. Itzinger: *Surf. Interface Anal.*, **48** (2015) 921–925.
- 20) T. Murata, Y. Goto, M. Sakairi, K. Fushimi and T. Kikuchi: *ECS Trans.*, **33** (2011) 57–63.
- 21) S. Hashizume, T. Nakayama, M. Sakairi and K. Fushimi: *Zairyo-to-Kankyo*, **60** (2011) 196–201.
- 22) J. P. Kollender, M. Voith, S. Schneiderbauer, A. I. Mardare and A. W. Hassel: *J. Electroanal. Chem.*, **740** (2015) 53–60.
- 23) J. P. Kollender, A. I. Mardare and A. W. Hassel: *Electrochim. Acta*, **179** (2015) 32–37.
- 24) K. Summers and D. Chidambaram: *J. Electrochem. Soc.*, **167** (2020) 121501.
- 25) M. Bilal and M. Sakairi: *J. Adv. Res.*, **26** (2020) 43–51.
- 26) M. Bilal and M. Sakairi: *J. Electrochem. Soc.*, **167** (2020) 081501.
- 27) M. Bilal and M. Sakairi: *Materials Today Communications*, **26** (2021) 102053.
- 28) M. Sakairi, R. Sasaki, A. Kaneko, Y. Seki and D. Nagasawa: *Electrochim. Acta*, **131** (2014) 123–129.
- 29) M. Chiba, S. Saito, H. Takahashi and Y. Shibata: *J. Solid State Electrochem*, **19** (2015) 3463–3471.
- 30) R. I. Revilla and I. D. Graeve: *J. Electrochem. Soc.*, **165** (2018) C532.



Kei Sakata  
Japan International Consultants  
for Transportation Co., Ltd.



Muhammad Bilal  
Department of Chemistry, Lehigh University



Masatoshi Sakairi  
Faculty of Engineering,  
Hokkaido University. Ph. D. (Eng.)



Takuya Murata  
Research & Development Division,  
UACJ Corporation